

MHD Instabilities in Reduction Cells

It is easier to write ten volumes on theoretical principles than
to put one into practice.

Tolstoy

The amount of energy required to reduce alumina to aluminium in electrolysis cells is staggering. In North America, for example, around 2% of all generated electricity is used to produce aluminium. Worldwide, around 2×10^{10} kg of aluminium are produced annually, and this requires in excess of 10^{11} kWh p.a. The corresponding electricity bill is around $\text{£}10^{10}$ p.a.! Yet much of this energy (around one half) is wasted in the form of I^2R heating of the electrolyte used to dissolve the alumina. Needless to say, strenuous efforts have been made to reduce these losses, mostly centred around minimising the volume of electrolyte. However, the aluminium industry is faced with a fundamental problem. When the volume of electrolyte is reduced below some critical threshold, the reduction cell becomes unstable. It is this instability, which is driven by MHD forces, which is the subject of this chapter.

11.1 Interfacial Waves in Aluminium Reduction Cells

11.1.1 Early attempts to produce aluminium by electrolysis

It is not an easy matter to produce aluminium from mineral deposits. The first serious attempt to isolate elemental aluminium was that of Humphrey Davy, Faraday's mentor at the Royal Institution. (In fact, Davy's preferred spelling – aluminum – is still used today in North America.) In 1809 he passed an electric current through fused compounds of aluminium and into a substrate of iron. Although an alloy of aluminium and iron resulted in place of the pure aluminium he sought, Davy had at least managed to prove that aluminium oxide was indeed reducible.

Oersted, and later Wöhler, set aside electricity and concentrated on chemical means of isolating aluminium. By 1827 Wöhler was able to produce small quantities of aluminium powder by displacing the metal

from its chloride using potassium. Later, in the 1850s, potassium was replaced by sodium, which was cheaper, and aluminium fluoride was substituted for the more volatile chloride. Wöhler's laboratory technique had at last become commercially viable and the industrial production of aluminium began. However, those chemical processes were all swept aside by the revolution in electrical technology initiated by Faraday. In particular, the development of the dynamo made it possible to produce aluminium by electrolysis.

The electrolytic route was first proposed by Robert Bunsen in 1854, but it was not until 1886 that a continuous commercial process was developed. It was a 22-year-old college student from Ohio, Charles Martin Hall, and the Frenchman Paul Héroult who made this breakthrough: the Frenchman as a result of good fortune (which he had the wit to pursue), and the American as a result of systematic enquiry. Hall and Héroult realised that molten cryolite, a mineral composed of fluorine, sodium and aluminium, readily dissolves alumina and that a current passed through the solution will decompose the alumina, leaving the cryolite unchanged. Full commercial production of aluminium began on Thanksgiving Day 1888 in Pittsburgh in a company founded by Hall. An example of an early Hall–Héroult reduction cell is shown in Figure 11.1(a). Remarkably, over a century later, the process is virtually unchanged.

11.1.2 The instability of modern reduction cells

Today almost all aluminium is produced by electrolysis, and the cells which are used look remarkably similar to those envisaged by Hall and Héroult. A schematic of a modern cell is shown in Figure 11.1(b). A large vertical current, perhaps 300 kA, flows downward from the carbon anode, passing first through the electrolytic layer (where it reduces the alumina) and then through a liquid aluminium pool before finally being collected at the carbon cathode at the base of the cell. The liquid layers are broad and shallow, perhaps 4 m × 10 m in plan, yet only a few centimetres deep.

The aluminium is an excellent conductor, the carbon a moderate one and the electrolyte (cryolite) a very poor conductor. Consequently, most of the electrical energy consumed by the cell is lost in Ohmic heating of the cryolite. In fact, these losses are vast, and there is considerable incentive to lower the resistance of the electrolyte layer by reducing its thick-

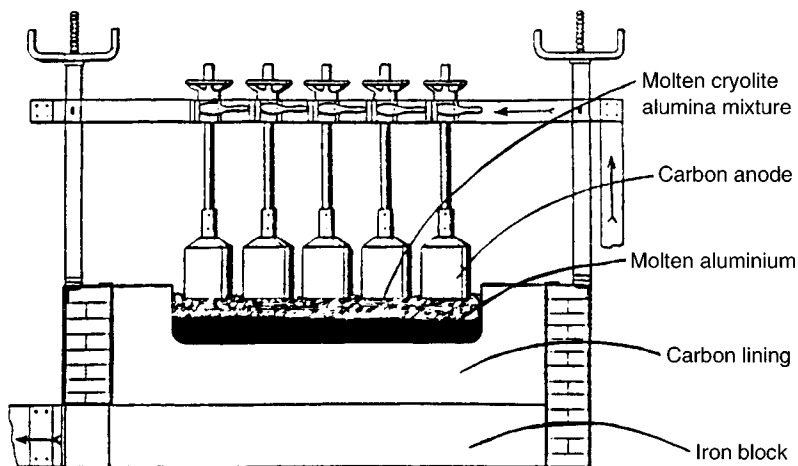


Figure 11.1 (a) A schematic of a 1920s reduction cell.

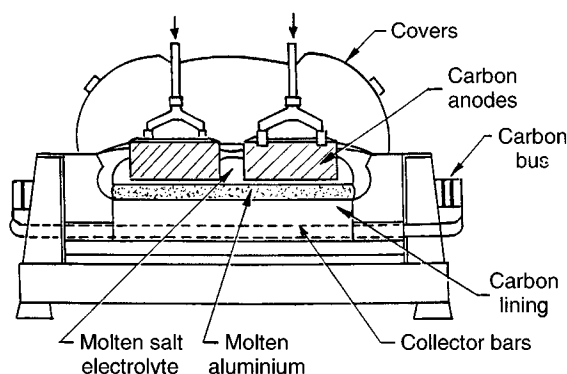


Figure 11.1 (b) A modern reduction cell.

ness. (Note the difference in electrolyte thickness in Figures 11.1(a) and 11.1(b).)

The energy problem aside, this process works reasonably well. However, there is one fundamental problem. It turns out that unwanted disturbances are readily triggered at the electrolyte–aluminium interface (Figure 11.2). In effect, these are long-wave-length, interfacial gravity waves, modified by the intense magnetic and electric fields which pervade the cell. Under certain conditions these disturbances are observed to grow, disrupting the operation of the cell. These instabilities have been

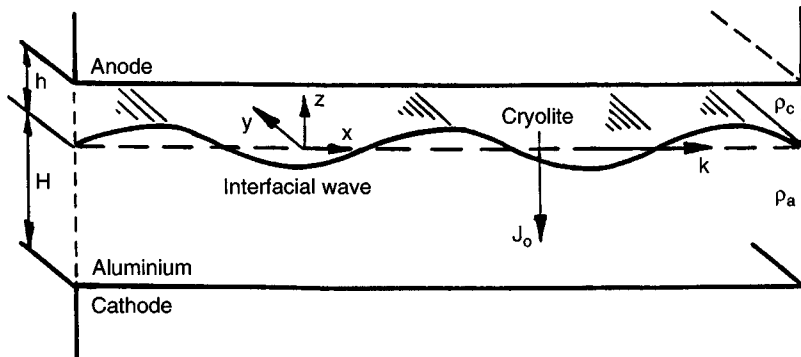


Figure 11.2 Interfacial waves in a reduction cell.

the subject of much research over the last two decades, since they represent the greatest single impediment to increasing the energy efficiency of these cells. In particular, the cryolite depth, h , must be maintained above a certain critical value to ensure stability, and this imposes a large energy penalty. Indeed, one aluminium company has estimated that each millimetre of cryolite costs them \$1 million per year in waste heat!

To some extent, the mechanism of the instability is clear. Tilting the interface causes a perturbation in current, \mathbf{j} . Excess current is drawn into the aluminium at those points where the thickness of the highly resistive cryolite is reduced, and less current is drawn at points where the electrolyte depth is increased. Since the carbon cathode is much more resistive than the aluminium, these perturbations in vertical current feed into the aluminium but do not penetrate the cathode. In the long-wavelength approximation ($kh \rightarrow 0$, k being the wavenumber) the perturbed current in the electrolyte is purely vertical while that in the aluminium is horizontal (to leading order in kh). This perturbation in current is shown in Figure 11.3 for the simplest of wave shapes.

Now the change in current causes a perturbation in the Lorentz force, $\delta\mathbf{F} = \mathbf{j} \times \mathbf{B}_0 + \mathbf{J}_0 \times \mathbf{b}$. In the long-wavelength limit, the dominant contribution to $\delta\mathbf{F}$ can be shown to be $\mathbf{j} \times \mathbf{B}_z$, where \mathbf{B}_z is the vertical component of the ambient magnetic field in the cell (see Section 3 of this chapter). The key question is, therefore, whether or not this change in Lorentz force amplifies the initial motion.

After many years of research, this issue was finally resolved by Sneyd & Wang (1994) and Bojorevics & Romerio (1994). Subsequently, their analyses were generalised by Davidson & Lindsay (1998). These authors all

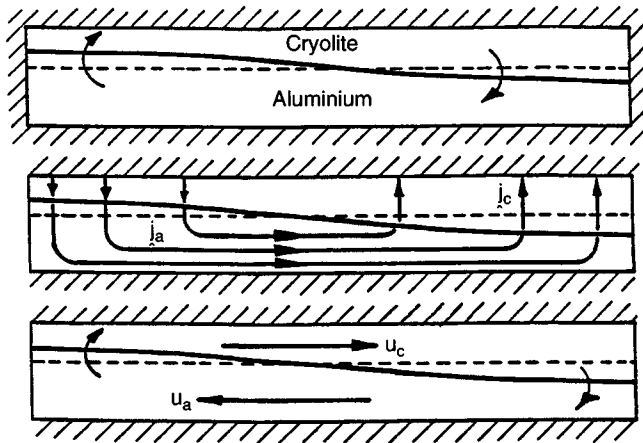


Figure 11.3 Perturbations in current caused by a movement of the interface. In the long-wave-length limit the perturbation current, \mathbf{j} , is largely vertical in the cryolite and horizontal in the aluminium. The 'sloshing' motion in the two liquids is largely horizontal.

simplify the geometry to that of a closed, rectangular domain (i.e. a shoe-box), as shown in Figure 11.2. Sneyd & Wang start by noting that, in the absence of a magnetic field, the interface may support an infinite number of conventional standing waves. The normal modes associated with these form an orthogonal set of functions, so that one can represent an arbitrary disturbance of the interface as the superposition of many such gravitational modes. When the Lorentz force is absent, these modes are decoupled. However, when the Lorentz force is taken into account, certain gravitational modes are coupled. That is, the redistribution of current caused by one mode gives rise to a Lorentz force which, when Fourier-decomposed, can excite many other modes. This leads to a coupled set of equations of the form

$$\ddot{\mathbf{x}} + \mathbf{\Omega}\mathbf{x} = \hat{\varepsilon}\mathbf{K}\mathbf{x}, \quad \hat{\varepsilon} = J_0 B_z / \rho_a H \quad (11.1)$$

Here \mathbf{x} is a column vector which represents the amplitudes of the gravitational modes, $\mathbf{\Omega}$ is diagonal with elements equal to the square of the conventional gravitational frequencies, H and ρ_a are the depth and density of the aluminium, respectively, and \mathbf{K} is the interaction matrix which arises from $\mathbf{j} \times \mathbf{B}_z$. Now \mathbf{K} is skew-symmetric and so complex eigenvalues, and hence instabilities, are guaranteed when $\hat{\varepsilon}$ is large. Unfortunately

however, (11.1) sheds little light on the all-important instability mechanism. Consequently, before going on to describe the instability in detail, we shall discuss a simple mechanical analogue which highlights the basic instability mechanism. This is due to Davidson & Lindsay (1998) and relies on the fact that, in the long-wavelength limit, the motion in the aluminium is purely horizontal (Figure 11.3).

11.2 A Simple Mechanical Analogue for the Instability

Suppose we replace the liquid aluminium by a thin, rigid, aluminium plate attached to the centre of the anode by a light rigid strut. The strut is pivoted at its top and so the plate is free to swing as a compound pendulum about two horizontal axes, x and y (Figure 11.4a). Let the plate have thickness H , lateral dimensions L_x , L_y and density ρ_a . The gap h between the plate and the anode is filled with an electrolyte of negligible inertia and poor electrical conductivity. A uniform current density, J_0 , passes vertically downward into the plate and is tapped off at the centre of the plate. Finally, suppose that there is an externally imposed vertical magnetic field B_z .

Evidently, we have replaced one mechanical system (the cell), which has an infinite number of degrees of freedom, with another which has only two degrees of freedom. However, electrically the two geometries are alike. Moreover, the nature of the motion in the two cases is not dissimilar. In both systems we have movement of the aluminium associated with tilting of the electrolyte–aluminium interface. In a cell this takes the form of a ‘sloshing’ back and forth of the aluminium as the interface tilts first one way and then the other (Figure 11.3).

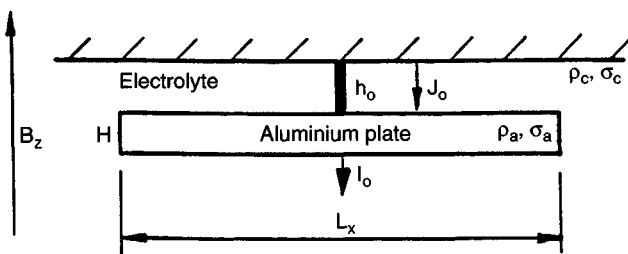


Figure 11.4 (a) The compound pendulum shown here contains all of the essential physics of the reduction cell instability.

Let θ_x and θ_y be the angles of rotation of the plate measured about x and y axes. Then it is not difficult to show that, as a result of these rotations, the perturbation of the current I in the aluminium plate is given by

$$\delta I_x = \frac{J_0 L_y \theta_y}{2h} [(L_x/2)^2 - x^2]$$

$$\delta I_y = -\frac{J_0 L_x \theta_x}{2h} [(L_y/2)^2 - y^2]$$

The perturbation in the Lorentz force $\mathbf{j} \times \mathbf{B}_z$ can be calculated from these expressions and the equations of motion for the compound pendulum then follow. They are

$$\ddot{\gamma}_x + \omega_x^2 \gamma_x = -(J_0 B_z / \rho_a H) \gamma_y = -\hat{\varepsilon} \gamma_y \quad (11.2a)$$

$$\ddot{\gamma}_y + \omega_y^2 \gamma_y = +(J_0 B_z / \rho_a H) \gamma_x = \hat{\varepsilon} \gamma_x \quad (11.2b)$$

where $\gamma_x = \theta_x / L_x$, $\gamma_y = \theta_y / L_y$ and ω_x , ω_y are the conventional gravitational frequencies of the pendulum. Note the similarity to (11.1). If we look for solutions of the form $\gamma \sim \exp(i\omega t)$ we find oscillatory solutions for small values of $\hat{\varepsilon} = J_0 B_z / \rho_a H$ and exponential (unstable) solutions for large $\hat{\varepsilon}$.

Figure 11.4(b) shows the movement of ω^2 in the complex plane as $\hat{\varepsilon}$ is increased. The two natural frequencies ω_x^2 and ω_y^2 move along the real axis until they meet. At this point, they move off into the complex plane and an instability develops. The important points to note are:

1. The tendency for instability depends only on the magnitude of $J_0 B_z / \rho_a H$ and on the natural gravitational frequencies ω_x and ω_y .

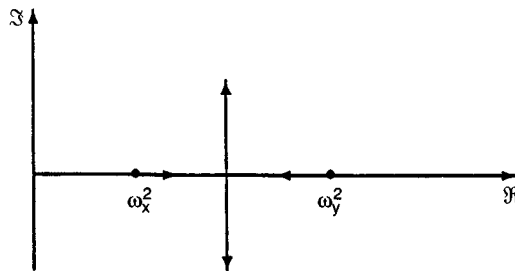


Figure 11.4 (b) Variations of ω^2 with $J_0 B_z$ in the complex plane for the pendulum.

2. To minimise the danger of an instability it is necessary to keep $J_0 B_z / \rho_a H$ low and the gravitational frequencies well apart. The closer the natural frequencies are, the lower the threshold value of $J_0 B_z$ at which an instability appears. (Circular and square plates are unstable for vanishingly small values of $J_0 B_z$.)
3. The system is unstable whenever

$$\frac{J_0 B_z}{\rho_a H} \geq \frac{1}{2} |\omega_x^2 - \omega_y^2|$$

4. When $\hat{\varepsilon}$ is large the unstable normal mode corresponds to a rotating, tilted plate.

Very similar behaviour is seen in reduction cells governed by (11.1). In particular, the sensitivity of reduction cells to the destabilising influence of $J_0 B_z$ depends on the initial separation of the gravitational frequencies. The closer the gravitational frequencies, the lower the stability threshold. Moreover, unstable waves frequently correspond to a rotating, tilted interface.

The physical origin of the instability of the pendulum is now clear. Tilting the plate in one direction, say θ_x , produces a horizontal flow of current in the aluminium which interacts with B_z to produce a horizontal force δF_x , which is perpendicular to the movement of the plate and in phase with θ_x . This tilting also produces a horizontal velocity, u_y , which is $\pi/2$ out of phase with the force δF_x and mutually perpendicular to it. Two such tilting motions in perpendicular directions can reinforce each other, with the force from one doing work on the motion of the other. This is the instability mechanism of the pendulum, and essentially the same thing happens in a reduction cell.

We may think of the Lorentz force as playing two rôles. In the first instance it modifies the gravitational frequencies, pulling them together on the real axis. Once these frequencies coincide, so that the plate oscillates at the same frequency in two directions, the Lorentz force adopts a second rôle in which it supplies energy to the pendulum. Unstable motion then follows.

A simple energy argument shows why, whenever the plate oscillates with a single frequency in two perpendicular directions, an instability is inevitable. From the expressions for δI_x and δI_y we can calculate the Lorentz force $\delta \mathbf{F}$ and hence the rate of work done by the force, $\delta \mathbf{F} \cdot \mathbf{u}$,

$$W = \delta \mathbf{F} \cdot \mathbf{u} = J_0 B_z L_x L_y [L_y^2 \theta_x \dot{\theta}_y - L_x^2 \theta_y \dot{\theta}_x] / 12 \quad (11.3)$$

Now suppose that θ_x and θ_y both oscillate at frequency ω , but are $\pi/2$ out of phase. Then the time-averaged value of \dot{W} is non-zero, implying unstable motion.

Note that this *instability mechanism* is independent of the action of gravity. That is, provided the plate can oscillate at the same frequency in two directions, it will become unstable. (Circular and square plates are unstable at arbitrarily small values of B_z .) The *stability threshold*, on the other hand, does depend on gravity, in that it is dependent on the initial separation of the gravitational frequencies.

We now return to reduction cells. We shall see that interfacial waves are described by the wave-like differential equation

$$\frac{\partial^2 \mathbf{q}}{\partial t^2} - c^2 \nabla^2 \mathbf{q} = \omega_B^2 [\hat{\mathbf{e}}_z \times \mathbf{q}]_P \quad (11.4)$$

where \mathbf{q} is the horizontal mass flux in the cryolite, $\omega_B^2 = J_0 B_z / (\rho_c H + \rho_a h)$ and $c^2 = (\rho_a - \rho_c)g / ((\rho_c/h) + (\rho_a/H))$. The subscript P on the term $\hat{\mathbf{e}}_z \times \mathbf{q}$ implies that we take only the irrotational (i.e. potential) component of $\hat{\mathbf{e}}_z \times \mathbf{q}$. This equation is valid quite generally and makes no assumption regarding the existence or shape of the lateral boundaries. Also, note that all of the electromagnetic effects are captured by the single parameter ω_B^2 . There are four special cases of interest.

- (i) When $\omega_B = 0$ we recover the standard wave equation for interfacial disturbances,

$$\frac{\partial^2 \mathbf{q}}{\partial t^2} - c^2 \nabla^2 \mathbf{q} = 0$$

- (ii) If ω_B is non-zero, and we look for solutions in the channel $0 < x < L$, then we find unstable travelling waves.
- (iii) For a closed circular domain, (11.4) yields unstable standing waves for vanishingly small values of ω_B . (Remember, a circular pendulum is unstable for vanishingly small $J_0 B_z$.) Moreover, the unstable normal mode corresponds to a rotating, tilted interface, just like that of the pendulum.
- (iv) If we place (11.4) in a rectangular domain we recover the matrix equation of Sneyd & Wang (1994):

$$\ddot{\mathbf{x}} + \Omega \mathbf{x} = \hat{\mathbf{e}} \mathbf{K} \mathbf{x}, \quad \hat{\mathbf{e}} = J_0 B_z / \rho_a H$$

where the coupling matrix, \mathbf{K} , is skew-symmetric and Ω is diagonal with elements equal to the square of the gravitational wave frequencies. (Note the similarity to (11.2).) We now set about deriving (11.4).

11.3 Simplifying Assumptions

A model of the cell is shown in Figure 11.2. The undisturbed depths of cryolite and aluminium are h and H , respectively, and the unperturbed current flow is purely vertical and has magnitude J_0 . We use a Cartesian coordinate system, (x, y, z) , where the positive direction of z is upward and the origin for z lies at the undisturbed interface. On occasion we shall refer to cells which are rectangular in plan view, and these are given dimensions L_x and L_y . However, much of the analysis can be applied to any shape of cell.

We take the characteristic time-scale for the wave motion to be much greater than the diffusion time of the magnetic field. That is, we make the pseudo-static approximation $\mu\sigma uh \ll 1$, where μ is the permeability, σ is the conductivity, and u is a typical velocity. Thus, each time the interface moves, the current immediately relaxes to a new equilibrium distribution. Ohm's law is then

$$\mathbf{J} = \sigma \mathbf{E} = -\sigma \nabla \Phi, \quad \nabla^2 \Phi = 0$$

We are concerned only with linear stability, and so we consider infinitesimal perturbations of the interface of the form $z_s = \eta$, $\eta \ll h, H$. The corresponding distributions of \mathbf{J} and \mathbf{B} are

$$\mathbf{J} = \mathbf{J}_0 + \mathbf{j} = -J_0 \hat{\mathbf{e}}_z - \sigma \nabla \phi, \quad \mathbf{B} = \mathbf{B}_0 + \mathbf{b}$$

and the boundary conditions on \mathbf{J} arise from the ranking of the conductivities. That is,

$$\sigma_a \gg \sigma_{\text{carbon}} \gg \sigma_c \quad (11.5)$$

Here the subscripts 'a' and 'c' refer to the aluminium and cryolite. It is not difficult to show that (11.5) requires $\phi_c = 0$ on $z = h$ and $\partial\phi_a/\partial z = 0$ on $z = -H$. Here ϕ is the perturbation in the electrostatic potential. The first of the boundary conditions states that the anode potential is fixed, while the second ensures that \mathbf{j} does not penetrate into the cathode blocks.

We shall assume that the fluid is inviscid, that surface tension can be ignored, and that there is no background motion in the unperturbed state. The first of these assumptions means that our equations of motion cannot mimic the damping of high-wavenumber perturbations which occur in practice. To compensate for this, we simply ignore those modes whose wavelengths are shorter than a certain (small but arbitrary) value. The last of the three assumptions (i.e. $\mathbf{u}_0 = 0$) greatly simplifies the stability analysis. However, this simplification does severely limit

the allowable distributions of \mathbf{B}_0 . That is, to ensure that the perturbation occurs about an equilibrium configuration, we must satisfy $\nabla \times (\mathbf{J}_0 \times \mathbf{B}_0) = \mathbf{0}$. Given our assumed distributions of \mathbf{J}_0 , we require \mathbf{B}_0 to be of the form

$$\mathbf{B}_0 = (B_x(x, y), B_y(x, y), B_z) \quad (11.6)$$

where B_z is spatially uniform. We shall assume that all three components of \mathbf{B}_0 are of the same order of magnitude. From Ampere's law, $\nabla \times \mathbf{B} = \mu \mathbf{J}$, which implies that $B_x \sim B_y \sim B_z \sim \mu J_0 L$ where L is a typical lateral dimension.

Our final assumption relates to the aspect ratio of the liquid layers. We shall assume that $kh \ll 1$, where k is a typical wavenumber. In effect, we use the shallow-water approximation. This leads directly to a number of simplifying features. In particular, as a result of the shallow-water approximation, and to leading order in kh , it may be shown that:

- (a) \mathbf{j} is vertical in the cryolite;
- (b) \mathbf{j} is horizontal in the aluminium and is uniformly distributed across that layer;
- (c) the perturbed Lorentz force acting on the cryolite may be neglected;
- (d) the velocity in each layer is uniform in z and horizontal;
- (e) the dominant contribution to the perturbed Lorentz force in the aluminium is $\mathbf{j} \times (B_z \hat{\mathbf{e}}_z)$.

In fact, it is not difficult to see how these simplifications arise. Consider the situation shown in Figure 11.3, where the disturbance has a long wavelength. Approximations (a) and (b) are purely geometric and are a consequence of the ranking of the conductivities. That is, the dominant resistance to the flow of current is the thin sheet of cryolite, so that the current passes directly downward through this layer (condition (a)). The aluminium, which is a very good conductor, is almost an equipotential surface, so that spatial variations of J_z in the cryolite (due to undulations of the interface) lead to a 'shorting' of the perturbed current through the aluminium. This 'shorted' current is almost purely horizontal (condition (b)). The neglect of the perturbed Lorentz force in the cryolite (condition (c)) stems from the fact that $\mathbf{j}_c \ll \mathbf{j}_a$, which in turn arises from the aspect ratio $kh \ll 1$. The uniformity of the velocity in the two fluid layers (condition (d)) follows from the fact that the Lorentz force in the aluminium is independent of depth.

This leaves only simplification (e) to justify, and here there is some subtlety in the argument. Using subscripts H and V to indicate horizontal

and vertical components of \mathbf{J} and \mathbf{B} , it seems reasonable to neglect $\mathbf{j}_H \times \mathbf{B}_H$ and $\mathbf{j}_V \times \mathbf{B}_H$ because the former is vertical and so merely perturbs the vertical pressure gradient, while the latter is much smaller than $\mathbf{j}_H \times \mathbf{B}_V$, by virtue of (b). Finally, the neglect of $\mathbf{b} \times \mathbf{J}_0$ relies on the fact that $|\mathbf{b}|$ is of order $|\mu \mathbf{j}_H H|$, while $|\mathbf{B}_0|$ is of order $\mu J_0 L_x$, so that $|\mathbf{J}_0 \times \mathbf{b}|$ is of order kH smaller than $|\mathbf{j} \times \mathbf{B}_V|$.

11.4 A Shallow-Water Wave Equation and Key Dimensionless Groups

We now derive a dynamic equation for interfacial waves. This equation (11.4) is more general than the ‘mode-by-mode’ description of (11.1) in that it makes no assumption regarding the existence or shape of lateral boundaries. The derivation is long and somewhat technical, and so the impatient reader may wish to jump directly to the end result, which is equation (11.18).

11.4.1 A shallow-water wave equation

We start with conventional shallow-water theory. It is not difficult to show that, to second order in kH , the pressure in each layer is hydrostatic. As a consequence, we may apply the conventional shallow-water equation to each layer in turn. This is a two-dimensional equation for the horizontal motion:

$$\rho \frac{D\mathbf{u}_H}{Dt} + \rho g \nabla H_a = -\nabla P_0 + \mathbf{F}_H$$

Here $H_a(x, y)$ is the aluminium depth, P_0 is the interfacial pressure, and \mathbf{F}_H is the horizontal body force in each layer. The unfamiliar term on the left arises from the horizontal gradient in pressure. For example, the pressure at the base of the aluminium layer is $P_0 + \rho_a g H_a$, so that the horizontal pressure force at the base of the layer is $-\nabla P_0 - \rho_a g \nabla H_a$. Similarly, the horizontal pressure force at the top of the cryolite layer is $-\nabla P_0 + \rho_c g \nabla H_c = -\nabla P_0 - \rho_c g \nabla H_a$.

Note that, since \mathbf{F}_H is independent of z (to leading order in kH), our shallow-water equation is a strictly two-dimensional equation of motion. We now linearise our equation of motion about a base state of zero background motion. Taking $H_a = H + \eta(x, y, t)$, we obtain

$$\rho \frac{\partial \mathbf{u}_H}{\partial t} + \rho g \nabla \eta = -\nabla P_0 + \mathbf{F}$$

Although \mathbf{u}_H is a two-dimensional velocity field, vertical movement of the interface means that the two-dimensional divergences of \mathbf{u}_{aH} and \mathbf{u}_{cH} are both non-zero. In fact, it is readily confirmed that (figure 11.5)

$$\nabla \cdot (H\mathbf{u}_a) = -\nabla \cdot (h\mathbf{u}_c) = -\frac{\partial \eta}{\partial t}$$

(Here we have dropped the subscript H for convenience.)

Next, we replace \mathbf{u}_a and \mathbf{u}_c by the volume fluxes $\mathbf{q}_a = H\mathbf{u}_a$ and $\mathbf{q}_c = -h\mathbf{u}_c$. Also, by virtue of condition (c) in Section 3 of this chapter, we may take $\mathbf{F}_c = 0$ (to leading order in kH). This is valid because, as we have seen, the current perturbation in the cryolite is an order of magnitude smaller than that in the aluminium. The governing equations become

$$\frac{\rho_c}{h} \frac{\partial \mathbf{q}_c}{\partial t} - \rho_c g \nabla \eta = \nabla P_0 \quad (11.7)$$

$$\frac{\rho_a}{H} \frac{\partial \mathbf{q}_a}{\partial t} + \rho_a g \nabla \eta = -\nabla P_0 + \mathbf{F}_a \quad (11.8)$$

$$\nabla \cdot \mathbf{q}_c = \nabla \cdot \mathbf{q}_a = -\frac{\partial \eta}{\partial t} \quad (11.9)$$

We now perform a so-called Helmholtz decomposition on \mathbf{q} : $\mathbf{q} = \mathbf{q}_R + \mathbf{q}_p$. That is, we divide \mathbf{q} into a solenoidal, rotational part and an irrotational component of finite divergence. The boundary conditions on \mathbf{q}_a and \mathbf{q}_c are that $\mathbf{q} \cdot \mathbf{n}$ vanishes at the boundary, S . An appropriate decomposition is therefore

$$\nabla \times \mathbf{q}_p = 0, \quad \nabla \cdot \mathbf{q}_p = -\frac{\partial \eta}{\partial t}, \quad \mathbf{q}_p \cdot \mathbf{n} = 0 \quad \text{on } S \quad (11.10)$$

$$\nabla \times \mathbf{q}_R = \nabla \times \mathbf{q}, \quad \nabla \cdot \mathbf{q}_R = 0, \quad \mathbf{q}_R \cdot \mathbf{n} = 0 \quad \text{on } S \quad (11.11)$$

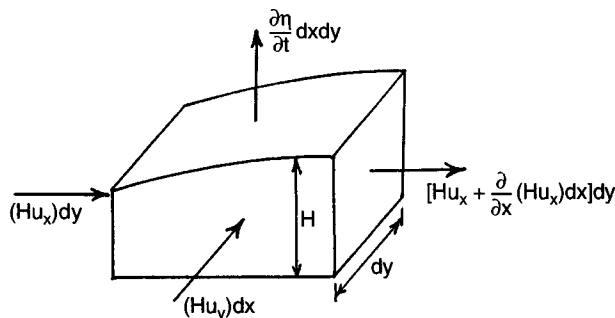


Figure 11.5 The horizontal divergence of \mathbf{u}_a .

Evidently, \mathbf{q}_R is zero in the electrolyte, while \mathbf{q}_P is the same in both layers: $\mathbf{q}_c = \mathbf{q}_p$; $\mathbf{q}_a = \mathbf{q}_p + \mathbf{q}_R$. We now rewrite (11.7) and (11.8) in terms of \mathbf{q}_P and \mathbf{q}_R , eliminate P_0 by adding the equations, and use (11.10) to express η in terms of \mathbf{q}_P . The resulting equation of motion is

$$\bar{\rho} \frac{\partial^2 \mathbf{q}_P}{\partial t^2} - \Delta \rho g \nabla^2 \mathbf{q}_P = \left[\frac{\partial \mathbf{F}_a}{\partial t} \right]_P \quad (11.12)$$

where $\bar{\rho} = \rho_c/h + \rho_a/H$ and $\Delta \rho = \rho_a - \rho_c$. The subscript P on the bracket implies that we take only the irrotational component of the corresponding term. Note that, when the Lorentz force is zero, we recover the conventional equation for interfacial waves in the shallow-water limit:

$$\boxed{\frac{\partial^2 \mathbf{q}_p}{\partial t^2} - c^2 \nabla^2 \mathbf{q}_p = 0, \quad c^2 = \Delta \rho g / \bar{\rho}} \quad (11.13)$$

We now evaluate \mathbf{j}_a , and hence \mathbf{F}_a , using the long-wavelength approximation. In the cryolite we have, to leading order in kH , $\partial^2 \Phi / \partial z^2 = 0$, from which

$$\Phi_c = \Phi_0 z / (h - \eta) + O(kh)$$

$$\mathbf{J}_c = -(J_0 \eta / h) \hat{\mathbf{e}}_z + O(kh)$$

This current passes into the aluminium, and so the boundary conditions on \mathbf{J}_{za} are

$$\mathbf{j}_{za} = -(J_0 \eta / h) \hat{\mathbf{e}}_z \quad \text{on } z = 0$$

$$\mathbf{j}_{za} = 0 \quad \text{on } z = -H$$

It is readily confirmed that the conditions of zero divergence and zero curl, as well as the boundary conditions given above, are satisfied by

$$\mathbf{j}_a = \mathbf{j}_H(x, y) - (1 + z/H)(J_0 \eta / h) \hat{\mathbf{e}}_z \quad (11.14)$$

Here \mathbf{j}_H is the horizontal component of the current density in the aluminium, which satisfies

$$\nabla \times \mathbf{j}_H = 0, \quad \nabla \cdot \mathbf{j}_H = \frac{J_0 \eta}{Hh}, \quad \mathbf{j}_H \cdot \mathbf{n} = 0 \quad \text{on } S \quad (11.15)$$

Comparing equation (11.15) with (11.10) we find that

$$\frac{\partial \mathbf{j}_H}{\partial t} = -\frac{J_0}{hH} \mathbf{q}_p \quad (11.16)$$

This is the key relationship which allows us to express the Lorentz force in terms of the fluid motion, and therefore it deserves some special attention. The physical basis for (11.16) is contained in Figure 11.3. When the interface tilts, there is a horizontal flow of current from the high to the low side of the interface. Simultaneously, there is a horizontal rush of the aluminium in the opposite direction. It is this coupling which lies at the heart of the instability, and which is expressed by (11.16).

We now invoke condition (e) of Section 11.3 which states that the leading term in the Lorentz force arises from the background component of B_z . Substituting for \mathbf{F}_a in (11.12) and introducing

$$\omega_B^2 = J_0 B_z / \bar{\rho} h H \quad (11.17)$$

we find, after a little algebra, that

$$\frac{\partial^2 \mathbf{q}_p}{\partial t^2} - c^2 \nabla^2 \mathbf{q}_p = \omega_B^2 [\hat{\mathbf{e}}_z \times \mathbf{q}_p]_p \quad (11.18)$$

Finally, to obtain the most compact version of our wave equation, it is convenient to introduce potentials for \mathbf{q}_p and $\mathbf{F}_p = \mathbf{F}_a - \mathbf{F}_R$.

$$\mathbf{q}_p = \nabla \phi_p, \quad \frac{\partial \mathbf{F}_p}{\partial t} = \bar{\rho} \omega_B^2 \nabla \Psi$$

Then (11.18) becomes

$$\frac{\partial^2 \phi_p}{\partial t^2} - c^2 \nabla^2 \phi_p = c^2 k_B^2 \Psi, \quad \nabla^2 \Psi = 0 \quad (11.19)$$

$$k_B^2 = \frac{J_0 B_z}{\Delta \rho g h H} \quad (11.20)$$

where k_B is defined as ω_B/c . The corresponding boundary conditions on ϕ_P and Ψ are

$$\nabla\phi_P \cdot \mathbf{n} = 0, \quad \nabla\Psi \cdot \mathbf{n} = (\nabla\phi_P \times \mathbf{n})_z \quad (11.21)$$

Note that the boundary condition on Ψ comes directly from (11.16) and from the definition of \mathbf{F}_P .

11.4.2 Key dimensionless groups

At last we are in a position to investigate cell stability! Solving (11.19) subject to boundary conditions (11.21) will determine the stability of the interface. Note that (11.19) is valid for any shape of domain, since we have made no assumptions about the lateral boundaries. We shall see that (11.19) can support both standing waves and travelling waves, and that both may go unstable.

Consider now a rectangular domain of size L_x, L_y . We can make (11.19) dimensionless by rescaling t according to $\hat{t} = k_B c t$ and \mathbf{x} according to $\hat{\mathbf{x}} = k_B \mathbf{x}$. In scaled units, (11.19) becomes

$$\ddot{\phi}_P - \nabla^2 \phi_P = \Psi, \quad \nabla^2 \Psi = 0$$

Evidently, the behaviour of interfacial waves in a rectangular domain is controlled only by (scaled) boundary shape, i.e. by $\hat{L}_x = k_B L_x$ and $\hat{L}_y = k_B L_y$. It follows that the stability threshold in a rectangular domain is uniquely determined by two dimensionless parameters,

$$\varepsilon^* = k_B^2 L_y^2 \frac{J_0 B_z L_y^2}{\Delta \rho g h H}, \quad r = L_x / L_y \quad (11.22a, b)$$

Here ε^* is a dimensionless version of $\hat{\varepsilon}$ introduced in (11.1). Later, when we show some examples of cell instabilities, we shall find it convenient to introduce a slightly different dimensionless measure of $J_0 B_z$.

$$\varepsilon = \left(\frac{2L_y}{\pi} \right)^4 \frac{J_0 B_z}{\Delta \rho g h H L_x L_y} = \left(\frac{2L_y}{\pi} \right)^4 \frac{k_B^2}{L_x L_y} \quad (11.22c)$$

11.5 Travelling Wave and Standing Wave Instabilities

Our shallow-water equation supports both travelling waves and standing waves. We shall show that both may become unstable.

11.5.1 Travelling waves

Consider an infinitely long channel of width L , say $0 < x < L$, as shown in Figure 11.6. The easiest way of identifying travelling waves is to write both Ψ and ϕ_P in the form

$$\phi_P = \hat{\phi}(x) \exp[j(\omega t - k_y y)]$$

and define a second wavenumber, k_x , through the expression $k_x^2 = (\omega^2/c^2) - k_y^2$. Then (11.19) gives the eigenvalue problem

$$\begin{aligned} \hat{\phi}'' + k_x^2 \hat{\phi} &= -k_B^2 \hat{\Psi}, & \frac{\partial \hat{\phi}}{\partial x} &= 0 & \text{on } x = 0, L \\ \hat{\Psi}'' - k_y^2 \hat{\Psi} &= 0, & \frac{\partial \hat{\Psi}}{\partial x} &= jk_y \hat{\phi} & \text{on } x = 0, L \end{aligned}$$

After a little algebra this yields a dispersion relationship for k_x in the form

$$\begin{aligned} 2(k_B L)^4 &\left[\cosh q \cos p - 1 + \frac{1}{2}(p/q - q/p) \sinh q \sin p \right] \\ &+ (p^2 + q^2)^2 (p/q) \sinh q \sin p = 0 \end{aligned} \quad (11.23)$$

where $p = k_x L$ and $q = k_y L$. When the Lorentz forces are zero ($k_B = 0$), this gives $k_x = m\pi/L$, which represents conventional travelling waves in a channel. For a finite value of k_B , and for an arbitrary wavenumber, k_y , we can always find a solution of (11.23) for which k_x is real. This represents stable travelling waves. However, (11.23) also supports unstable waves. That is, for real values of k_B and k_y , we can find complex values of k_x

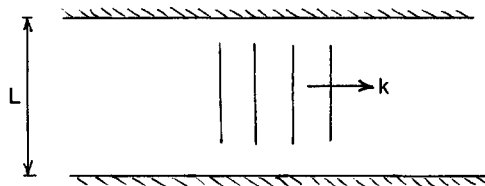


Figure 11.6 Travelling waves in a channel.

which satisfy (11.23). This leads to complex frequencies and therefore to unstable motion. Figure 11.7 shows the neutral stability curve for waves in the range $0 < q < 10$.

11.5.2 Standing waves in circular domains

We now consider waves in a closed, circular domain. This is of interest as it demonstrates the instability in a particularly simple way. Suppose the fluids occupy the domain $0 < r < R$, and consider solutions of the form

$$\phi_p = \hat{\phi}(r) \exp[j(\theta - \omega t)], \quad \Psi = \hat{\Psi}(r) \exp[j(\theta - \omega t)]$$

It is readily confirmed that (11.19) requires $\hat{\Psi}$ to be linear in r , $\hat{\Psi} = Ar$, and that $\hat{\phi}$ takes the form

$$\hat{\phi}(r) = BJ_1(kr) - (k_B^2/k^2)Ar, \quad k = \omega/c$$

where J_1 is the usual Bessel function. Boundary conditions (11.21) require

$$\hat{\phi}'(R) = 0, \quad \hat{\phi}(R) = jRA$$

which yields the dispersion relation

$$k_B^2 J_2(kR) = jk^2 J_1'(kR)$$

This requires that k is complex, and so the waves are unstable for all non-zero k_B . The key point, though, is that the interface near marginal stability is of the form

$$\eta \sim J_1(kr) \sin(\theta - \omega t)$$

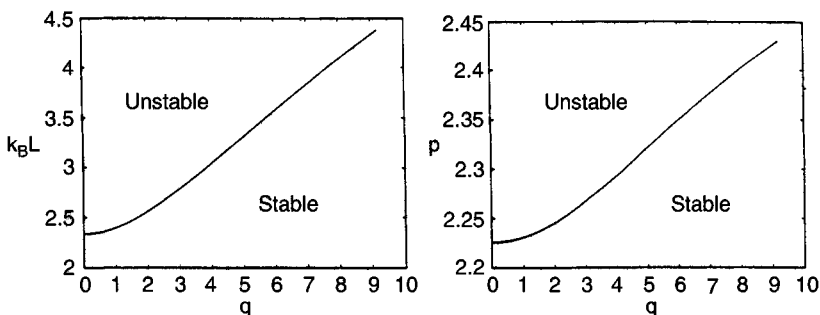


Figure 11.7 Neutral stability curves corresponding to (11.23).

which represents a rotating, tilted interface. This is precisely what is expected from the compound pendulum analogue.

11.5.3 Standing waves in rectangular domains

We now turn to rectangular domains. Here it is convenient to rewrite (11.19) in matrix form. This can be achieved by expanding \mathbf{q}_p in a set of orthogonal cosine functions ψ_i of the form

$$\begin{aligned}\mathbf{q}_p &= \sum \mathbf{q}_i = \sum k_i^{-1} x_i(t) \nabla \psi_i \\ \psi_i &= \psi_{mn} \sim \cos(m\pi x/L_x) \cos(n\pi y/L_y) \\ k_i^2 &= k_{mn}^2 = (m\pi/L_x)^2 + (n\pi/L_y)^2\end{aligned}$$

Here $x_i(t)$ are the amplitudes of the modes. Of course, ψ_i are just the gravitational modes in the absence of Lorentz forces, and k_i are the corresponding wavenumbers.

We now take the dot-product of (11.18) and $\nabla \psi_i$ and integrate over V . The result is

$$\ddot{x}_i(t) + \omega_{gi}^2 x_i = \omega_B^2 \sum K_{ij} x_j \quad (11.24)$$

where ω_{gi} are the gravitational frequencies and the interaction matrix K_{ij} has elements

$$k_i k_j K_{ij} = \int (\nabla \psi_j \times \nabla \psi_i)_z dV \quad (11.25)$$

We have normalized ψ_i such that

$$\int \psi_i^2 dV = 1 \quad (11.26)$$

Note that K_{ij} is skew-symmetric and has all of its diagonal elements equal to zero:

$$K_{ij} = -K_{ji} \quad (11.27)$$

Finally we truncate x_i at some suitably small wavenumber and rewrite (11.24) in matrix form:

$$\ddot{\mathbf{x}} + \boldsymbol{\Omega}_g \mathbf{x} = \omega_B^2 \mathbf{K} \mathbf{x} \quad (11.28)$$

Let us now consider some of the more general properties of (11.28). Consider the case where ω_B is much greater than the gravitational frequencies of the truncated system. In this case, (11.28) gives

$$\frac{d^4 \mathbf{x}}{dt^4} = -\omega_B^4 \mathbf{S}_1 \mathbf{x}, \quad \mathbf{S}_1 = -\mathbf{K}\mathbf{K} \quad (11.29)$$

The equivalent eigenvalue problem is

$$\mathbf{S}_1 \mathbf{x} = -(\omega/\omega_B)^4 \mathbf{x} = \lambda \mathbf{x} \quad (11.30)$$

Now \mathbf{S}_1 is real, symmetric and has positive diagonal elements. It follows that the eigenvalues, λ_i , are real and at least some of them are positive. We conclude, therefore, that for large ω_B at least some frequencies of our truncated system are complex.

Let us now return to the general eigenvalue problem represented by (11.28):

$$(\mathbf{\Omega}_g - \omega_B^2 \mathbf{K}) \mathbf{x} = \lambda \mathbf{x}, \quad \lambda = \omega^2 \quad (11.31)$$

Suppose that \mathbf{x} is truncated after N modes and that the diagonal elements of $\mathbf{\Omega}_g$ are arranged in order of increasing frequency from ω_{g1}^2 to ω_{gN}^2 . Then we may show that in the truncated system the eigenvalues, λ_i , have the following general properties:

- (a) $\omega_{g1}^2 \leq \text{Re}(\lambda) \leq \omega_{gN}^2$;
- (b) $\sum \lambda_i = \sum \omega_{gi}^2$;
- (c) λ_i/ω_B^2 are zero or purely complex if, $\omega_B^2 \gg \omega_{gN}^2$.

These properties are sufficient to define the general behaviour of λ . The first follows from the skew-symmetry of \mathbf{K} . That is, if \bar{x}_i is the complex conjugate of x_i , then

$$\sum_i (\omega_{gi}^2 - \lambda) |x_i|^2 = \omega_B^2 \sum_i \sum_j K_{ij} x_j \bar{x}_i$$

If we normalize the eigenvectors to have unit magnitude and take the complex conjugate of the transpose of this equation, we obtain

$$\text{Re}(\lambda) = \sum \omega_{gi}^2 |x_i|^2$$

Condition (a) then follows. Condition (b), on the other hand, arises from the fact that the sum of the eigenvalues equals the trace of $\mathbf{\Omega}_g - \omega_B^2 \mathbf{K}$, while condition (c) is a standard result for skew-symmetric matrices.

The situation is therefore clear. As ω_B is increased, the eigenvalues move along the real axis but remain within the limits $\omega_{g1}^2 < \lambda < \omega_{gN}^2$. At some critical value of ω_B two or more eigenvalues become complex (an inevitable consequence of condition (c)) and do so in the form of complex conjugate pairs (condition (b)). However, the real part of the

complex eigenvalues remain bounded by the least and largest gravitational frequency of the truncated set of modes (condition (a)).

We now present a simple numerical example which illustrates the phenomenon. We shall show that frequently it is not the pair of modes with the closest gravitational frequencies which go unstable first. Moreover, the modes which go unstable at the lowest value of $J_0 B_z$ need not be the most dangerous. Often the highest growth rates are observed in the pairs of modes which are the second or third to go unstable. Of course, it is the modes with the highest growth rates which are most likely to survive the friction which is inevitably present in any real flow. We start by rewriting (11.31) in dimensionless form. We use $k_1 = \pi/L_y$ as a characteristic (inverse) lengthscale and introduce $\hat{k}_i = k_i/k_1$, $\hat{\lambda} = \omega^2/(ck_1)^2$, and

$$\varepsilon = \left(\frac{2L_y}{\pi}\right)^4 \frac{J_0 B_z}{\Delta \rho g h H L_x L_y} = \left(\frac{2L_y}{\pi}\right)^4 \frac{\omega_B^2}{c^2 L_x L_y}$$

Consider the case $L_y/L_x = 0.3$, which is typical of a real cell. The trajectories of the eigenvalues in the complex plane are shown in Figure 11.8. Three ranges of ε are indicated, corresponding to $\varepsilon < 0.12$, $\varepsilon < 0.15$ and $\varepsilon < 0.20$. Figure 11.8(a) shows that, by $\varepsilon = 0.12$, one pair of eigenvalues has coalesced and moved into the complex plane. In fact, these complex eigenvalues first appear at $\varepsilon = 0.0577$, through the interaction of the $(3, 0)$ and $(0, 1)$ modes. (We classify the eigenvalues in terms of their mode number (m, n) when $\varepsilon = 0$). By $\varepsilon = 0.15$, the complex eigenvalues have returned to the real axis and a new pair of unstable frequencies have appeared. This arises from an interaction of a $(2, 0)$ mode with one of the pair of previously unstable eigenvalues. By $\varepsilon = 0.2$ two additional unstable pairs have appeared. One arises from the interaction of $(1, 1)$ and $(2, 1)$ modes, and the other through the interaction of the $(1, 0)$ mode with the second of the pair of previously unstable modes. The behaviour is summarised in Table 11.1.

Table 11.1. *Formation of unstable frequencies*

| Instability | Modes | Comments |
|-------------|---|-----------------------|
| First ... | $(3, 0) + (0, 1)$ | Restabilises |
| Second ... | $(2, 0) + \frac{1}{2}[(3, 0) + (0, 1)]$ | — |
| Third ... | $(1, 1) + (2, 1)$ | Furthest to the right |
| Fourth ... | $(1, 0) + \frac{1}{2}[(3, 0), (0, 1)]$ | Furthest to the left |

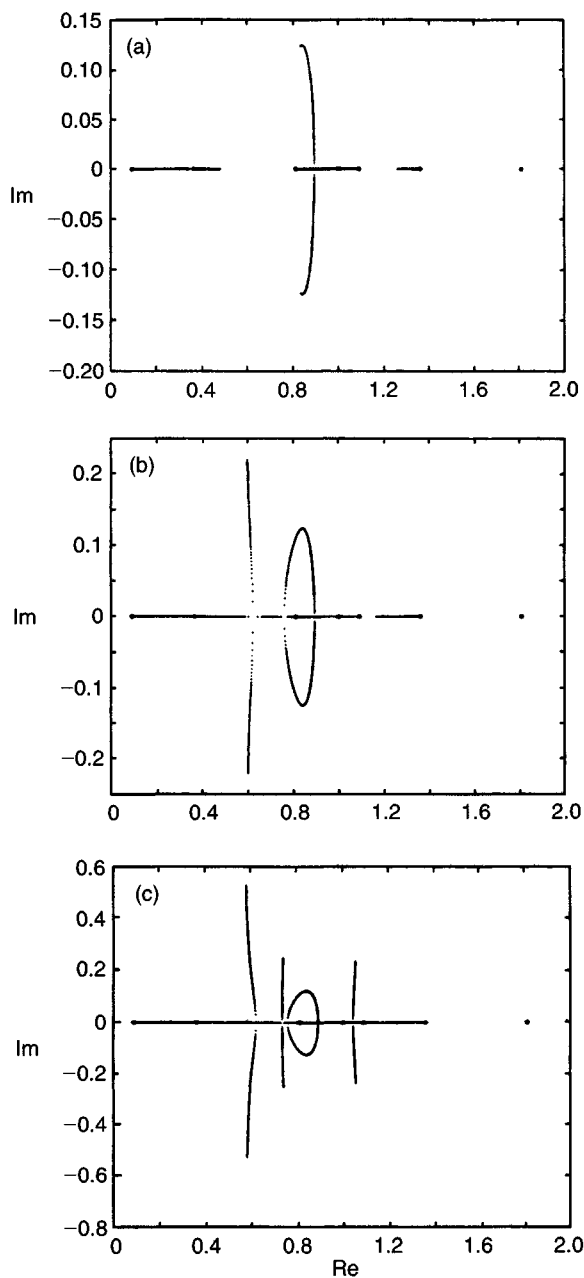


Figure 11.8 Instabilities in a rectangular cell, $L_y/L_x = 0.3$.

This simple example exhibits two interesting features. First, it is not the modes with the closest gravitational frequencies ω_{gi} which go unstable. In fact, the closest gravitational frequencies are the (0, 1) and (1, 1) modes, yet at no time do they combine to produce an instability. Second, by $\varepsilon = 0.2$, the largest growth rate is exhibited not by the first instability, but by the fourth one. Given that any real flow has dissipation, it is this last instability which is the most likely to appear in practice.

Notice that the first instability appears at quite low values of ε , $\varepsilon = 0.0577$ (i.e., $\omega_B L_y / c = 1.08$). The idea is that, while ω_B is still quite small, two adjacent frequencies might interact, converge and move off onto the complex plane. If the initial frequencies are close, this interaction is a local one, in the sense that it does not involve the other modes. This, in turn, leads to the idea that modes with close gravitational frequencies are dangerous. However, it is important to note that \mathbf{K} is very sparse. Indeed only around one in five mode-pairs are coupled. In general, then, relatively few modes exchange energy. It is not difficult to show that an instability cannot develop from these uncoupled modes, so it is only the separation of the coupled modes which is important. Thus a stability criterion based on keeping all gravitational modes apart is overly conservative. This point is of considerable practical importance.

11.6 Implications for Reduction Cell Design

There are many idealisations embedded in our stability analysis, and so it would be imprudent to consider it as representing an accurate working model of a real cell. Nevertheless, it does capture the key instability mechanism and so the broad conclusions of the model should be valid. It follows that if we wish to avoid instabilities it is sensible to:

- (i) choose the cell aspect ratio L_x/L_y to ensure that the natural frequencies of the dominant interfacial waves are well separated;
- (ii) minimise the ambient vertical field, B_z ;
- (iii) carefully control the fluid depths, h and H .

If we wish to eliminate the instability completely then more drastic action is required. One possibility is to introduce baffles into the liquid aluminium, whose function is to break up the long-wavelength sloshing motions. Another is to monitor the interface position continuously, and slowly tilt or move the anode in sympathy with any wave so as to keep the electrolyte thickness roughly uniform. This will prevent the build

up of large current perturbations and so remove the driving force for the instability. However, there are many practical problems associated with these modifications. Perhaps Tolstoy was right when he suggested that it is easier to hypothesise than to act.

Examples

- 11.1 The depth of the electrolyte in present-day reduction cells is around 5 cm. Estimate the annual savings which would result from reducing this by 1 cm.
- 11.2 There are at least three simple ways of eliminating the instability. Two are listed above. The third is to use sloping cathode blocks to continuously drain the aluminium and so avoid the build-up of a thick aluminium layer. Why do you think this has not been implemented?
- 11.3 Find the normal mode shape for the oscillations of the compound pendulum shown in Figure 11.5. Confirm that for large ε the mode consists of a rotating, tilted plate.
- 11.4 Give a simple physical explanation, based on the compound pendulum, why travelling wave instabilities in a channel are inevitable.